Supplemental Document

Optics EXPRESS

Model-based temporal unmixing towards quantitative photo-switching optoacoustic tomography: supplement

YAN LIU,[1] JONATHAN CHUAH,[1] YISHU HUANG,[2] ANDRE C. STIEL,[2,3] MICHAEL UNSER,[1,*] AND JONATHAN DONG[1]

[1] *Biomedical Imaging Group, École Polytechnique Fédérale de Lausanne, Station 17, 1015 Lausanne, Switzerland*
[2] *Institute of Biological and Medical Imaging, Helmholtz Zentrum München, Neuherberg, Germany*
[3] *Faculty of Biology and Pre-Clinical Medicine, University of Regensburg, Regensburg, Germany*
[*] *michael.unser@epfl.ch*

Supplement DOI: https://doi.org/10.6084/m9.figshare.28269245

Parent Article DOI: https://doi.org/10.1364/OE.550253

Model-Based Temporal Unmixing Towards Quantitative Photo-switching Optoacoustic Tomography: Supplement

This document provides supplementary information for the manuscript: Model-Based Temporal Unmixing Towards Quantitative Photo-switching Optoacoustic Tomography. In Section 1, we include the supporting tables and figures for the manuscript. In Section 2, we detail the model and computation of the fluence maps used for unmixing. In Section 3, we provide an additional simulation that shows the effectiveness of the regularization. In Section 4, we explain the estimation of the kinetic constants of the photo-switching proteins.

1. SUPPORTING TABLES AND FIGURES

We provide an extract of the key photo-physical properties of the reversibly switchable OA reporters (rsOAPs) used in the experiments in Table S1. For a summary of the complete properties of these reporters, refer to [1].

Name	τ_{OFF}	$\bar{k}$	$\varepsilon^{\mathrm{ON}}_{770\mathrm{nm}}$	$\varepsilon^{\mathrm{OFF}}_{770\mathrm{nm}}$
Unit	s	s^{-1}	$\mu\mathrm{M}^{-1}\mathrm{cm}^{-1}$	$\mu\mathrm{M}^{-1}\mathrm{cm}^{-1}$
*Re*BphP-PCM (Re)	0.18	3.85	0.07	0.002
*Dr*BphP-PCM (Dr)	0.70	0.99	0.04	0.004
*Rp*BphP1-PCM (Rp)	0.42	1.65	0.06	0.009

Table S1. Key photo-physical properties of the three rsOAPs used in the experiments: half time of the OFF switching cycle τ_{OFF}; kinetic constant $\bar{k}$ derived based on τ_{OFF}; molar extinction coefficients of the ON and OFF states $\varepsilon^{\mathrm{ON}}_{770\mathrm{nm}}$, $\varepsilon^{\mathrm{OFF}}_{770\mathrm{nm}}$ at 770nm (OFF-switching) wavelength.

We provide in Fig. S1 the OA signal during a typical OFF switching cycle in the numerical simulation of a phantom of beads described in section 3 in this Supplement. We observe that after 25 time steps (marked with a vertical gray dashed line), there is less useful information in the signal other than noise. Hence, only the first 25 frames of OA images are used in the reconstruction.

2. ESTIMATION OF THE LIGHT FLUENCE

A. Geometry of the Setup

The setup of our phantom experiment is illustrated in Fig. S2. The cylindrical agar phantom, which serves as the non-switching background, has a diameter of 27mm and is submerged in water to match the refractive indices. We inserted tubes of diameter 580 μm filled with solutions of photo-switching proteins inside the phantom. The illumination originates from five laser outlets that surround the body of the phantom such that the incident light can be assumed homogeneous and diffuse on the surface of the body of the cylinder.

B. Optical Parameters

The absorption coefficient μ_a of the background is calculated according to [2]

$$\mu_a(\lambda) = \ln 10 \cdot \varepsilon(\lambda)[\mathrm{cm}^{-1} \cdot \mathrm{mole}^{-1} \cdot \mathrm{L}] \cdot \frac{x\% \cdot 150[\mathrm{g} \cdot \mathrm{L}^{-1}]}{64500[\mathrm{g} \cdot \mathrm{mole}^{-1}]}, \tag{S1}$$

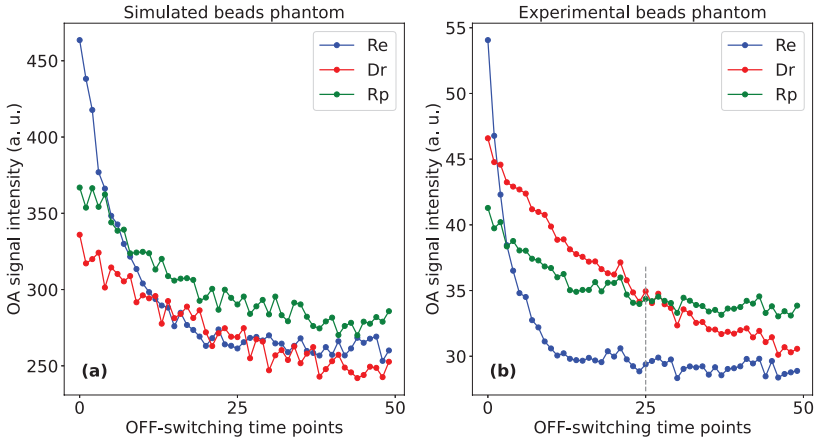

Fig. S1. Evolution of the OA signal during an OFF-switching cycle of 50 time points at three representative locations inside the three rsOAPs: Re (blue), Dr (red), and Rp (green) for the simulated (a) and experimental measurements (b) of a phantom of beads. The noise level in the measurements of the simulated beads phantom is 1% of its maximal intensity.

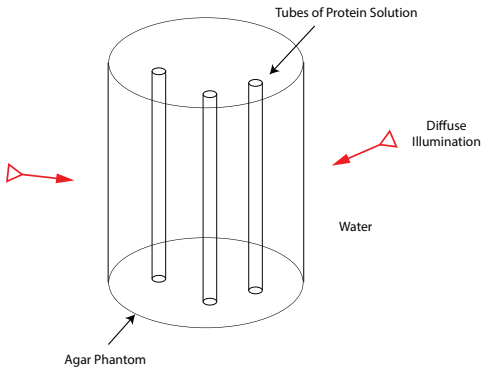

Fig. S2. Experimental setup of the phantom.

where $\lambda = 770$ nm is the OFF-switching wavelength, $\varepsilon(\lambda) = 1311.88[\mathrm{cm}^{-1} \cdot \mathrm{mole}^{-1} \cdot \mathrm{L} = \mathrm{cm}^{-1} \cdot \mathrm{M}^{-1}]$ is the molar extinction coefficient of blood at 770 nm, assuming the blood we used in the phantom to be mostly composed of deoxygenated hemoglobin (Hb), $x = 3$ is the percentage of blood used in the phantom, $150[\mathrm{g} \cdot \mathrm{L}^{-1}]$ is the typical mass concentration of hemoglobin within blood, and $64500[\mathrm{g} \cdot \mathrm{mole}^{-1}]$ is the molecular weight of hemoglobin. Using these values, the background is determined by $\mu_a^{\mathrm{bg}} = 0.21[\mathrm{cm}^{-1}]$.

The absorption coefficients of the protein species Re and Dr is calculated via [3]

$$\mu_a(\lambda) = \ln 10 \cdot \varepsilon(\lambda)[\mathrm{M}^{-1} \cdot \mathrm{cm}^{-1}] \cdot c[\mathrm{M}] \tag{S2}$$

from their molar concentration $c_{\mathrm{Re}} = 4.23 \times 10^{-6}$ [M], $c_{\mathrm{Dr}} = 3.71 \times 10^{-6}$ [M] and their respective molar extinction coefficients at 770nm $\varepsilon_{\mathrm{Re}}(770\mathrm{nm}) \approx 0.7 \times 10^5$ $[\mathrm{M}^{-1} \cdot \mathrm{cm}^{-1}]$, $\varepsilon_{\mathrm{Dr}}(770\mathrm{nm}) \approx 0.4 \times 10^5$ $[\mathrm{M}^{-1} \cdot \mathrm{cm}^{-1}]$. We thus have $\mu_a^{\mathrm{Re}} = 0.68\ \mathrm{cm}^{-1}$ and $\mu_a^{\mathrm{Dr}} = 0.34\ \mathrm{cm}^{-1}$.

We adopt a typical value of $10\ \mathrm{cm}^{-1}$ for the reduced scattering coefficient μ_s' of the background, which is composed of 3% intralipid as a scatterer.

C. Diffusion Equation

From the calculated optical parameters, we see that the light propagation within the sample is within the diffuse regime in which scattering is much stronger than absorption ($\mu_a \ll \mu_s'$). We thus adopt the diffusion equation Eq. (S3) complemented by the suitable boundary condition Eq. (S4) which describes the tissue/water interface to compute the light fluence distribution $\Phi(\mathbf{r})$

over a sample Ω as [4, 5]

$$\mu_a(\mathbf{r})\Phi(\mathbf{r}) - \nabla \cdot (D(\mathbf{r})\nabla\Phi(\mathbf{r})) = S(\mathbf{r}), \qquad \boldsymbol{r} \in \Omega, \tag{S3}$$

$$\Phi(\mathbf{r}) - 2D(\mathbf{r})\nabla\Phi(\mathbf{r}) \cdot \mathbf{n} = 0, \qquad \boldsymbol{r} \in \partial\Omega \tag{S4}$$

where Ω is a 3D domain, and $\mathbf{n}$ is the outward normal vector of the boundary. The illumination is described by a function $S(\mathbf{r})$. The diffusion coefficient $D(\mathbf{r})$ depends on the absorption coefficient $\mu_a(\mathbf{r})$ and the reduced scattering coefficient $\mu_s^{'}(\mathbf{r})$ according to

$$D(\mathbf{r}) = \frac{1}{3(\mu_a(\mathbf{r}) + \mu_s^{'}(\mathbf{r}))}. \tag{S5}$$

In the case of our agar cylinder phantom, we model the domain Ω with a cylinder of height H and diameter L (see Fig. S2), which leads to

$$\Omega = \left\{(x,y,z) | (z-z_c)^2 + (x-x_c)^2 \leq (L/2)^2, 0 \leq y - y_c \leq H\right\}. \tag{S6}$$

The incident diffuse illumination on the body of the phantom is approximated by a function $S(\mathbf{r})$ of constant-intensity I_0

$$\begin{aligned} S(x,y,z) &= I_0, \text{ if } (z-z_c)^2 + (x-x_c)^2 = (L/2)^2 \\ &= 0, \text{ else} \end{aligned} \tag{S7}$$

D. Numerical Implementation

D.1. Variational Formulation

We numerically solve Eq. (S3) and Eq. (S4) via the finite element method and we briefly summarize the key steps to achieve the variational formulation. First, multiply Eq. (S3) with a test function $v(\mathbf{r})$ from a suitable function space and integrate over Ω, obtaining

$$\int_\Omega \mu_a(\mathbf{r})\Phi(\mathbf{r})v(\mathbf{r})\mathrm{d}\boldsymbol{r} - \int_\Omega \nabla \cdot (D(\mathbf{r})\nabla\Phi(\mathbf{r}))v(\mathbf{r})\mathrm{d}\boldsymbol{r} = \int_\Omega S(\mathbf{r})v(\mathbf{r})\mathrm{d}\boldsymbol{r}. \tag{S8}$$

Then use integration by parts to get

$$\int_\Omega \mu_a(\mathbf{r})\Phi(\mathbf{r})v(\mathbf{r})\mathrm{d}\boldsymbol{r} + \int_\Omega D(\mathbf{r})\nabla\Phi(\mathbf{r}) \cdot \nabla v(\mathbf{r})\mathrm{d}\boldsymbol{r} - \int_{\mathrm{d}\Omega} (D\underbrace{\nabla\Phi(\mathbf{r}) \cdot \mathbf{n}}_{\frac{\Phi(\mathbf{r})}{2D}})v(\mathbf{r})\mathrm{d}s = \int_\Omega S(\mathbf{r})v(\mathbf{r})\mathrm{d}\boldsymbol{r}. \tag{S9}$$

Reorganize the terms and conclude with

$$\int_\Omega ((\mu_a\Phi(\mathbf{r}) - S(\mathbf{r}))\, v(\mathbf{r}) + D(\mathbf{r})\nabla\Phi(\mathbf{r}) \cdot \nabla v(\mathbf{r}))\mathrm{d}\mathbf{r} = \int_{\mathrm{d}\Omega} \frac{\Phi(\mathbf{r})v(\mathbf{r})}{2}\mathrm{d}s. \tag{S10}$$

D.2. Meshes

We represent the domain Ω with two type of meshes of uniform mesh elements. The first type is a grid composed of boxes with size determined by its physical size (Z, X, Y) and the number of sampling points $(N_\mathrm{z}, N_\mathrm{x}, N_\mathrm{y})$ in each dimension: $(Z/N_\mathrm{z}, X/N_\mathrm{x}, Y/N_\mathrm{y})$. This type is used in the construction of the forward model and the unmixing algorithm (due to matrix operations). The second type is a finite element mesh that discretizes the cylinder domain directly into tetrahedrons with mesh size Δs, which we choose to be $\max(Z/N_\mathrm{z}, X/N_\mathrm{x}, Y/N_\mathrm{y})/2$ to reach a balance between computational accuracy and speed (see Fig. S3 (a)). This is done using Gmsh, an open-source 3D finite element mesh generator [6]. This type of mesh is used to solve the diffusion equation. For computational speed, we precompute and save the 3D mesh with defined physical sizes and only load it when needed.

The relation between these two meshes is illustrated in Fig. S3 (b). To be precise, the box mesh tightly fits the cylinder. The conversion between the two meshes is necessary when we compute the fluence using optical parameter maps defined on a grid and when we cast the solution of the fluence from the finite element mesh to the grid. We use linear interpolation in both cases.

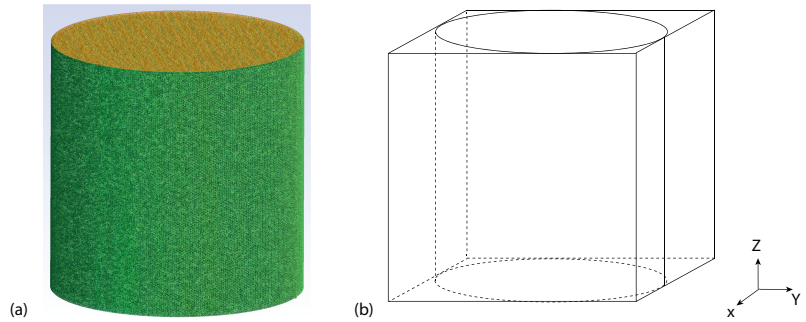

Fig. S3. (a) Finite-element mesh of a cylinder generated using Gmsh. (b) Relation between the grid and the finite-element mesh.

Algorithm S1. Algorithm to solve the diffusion equation using Fenicsx

1: **Input** $\mu_a(\mathbf{r})$, $\mu_s'(\mathbf{r})$, and $S(\mathbf{r})$ as 3D arrays
2: Define mesh and function space V of type "continuous Galerkin" of order 1
3: Convert $\mu_a(\mathbf{r})$, $\mu_s'(\mathbf{r})$, and $S(\mathbf{r})$ to functions in V
4: Assemble Eq. (S10) into a linear form $a(\Phi, v) = L(v)$
5: Solve the linear form to get solution ϕ_h
6: Convert the finite-element solution ϕ_h over a cylinder to a 3D box array ϕ^{3D} that contains ϕ_h
7: Slice a cross-section of ϕ^{3D} to obtain a 2D fluence map ϕ^{2D}
8: **Output** 2D array ϕ^{2D}

D.3. Solving the Equation

Eq. (S10) is solved using Fenicsx, an open-source library for the numerical solution of partial differential equations [7, 8]. We provide a summary in Algorithm S1.

Note that the finite-element solution ϕ_h is over a cylindrical domain We convert it to a 3D array that that tightly contains the cylinder. The output of the fluence computation is a 2D cross-sectional image of the original 3D map, which we use to construct the forward model as described in Fig. 2 of the manuscript.

3. EFFECTIVENESS OF THE REGULARIZATION

We show the effectiveness of the proposed regularization in our unmixing framework with the following simulation. We design a 2D numerical phantom of size (150×150)px in which we randomly insert three groups of disk targets of diameter between 7px and 12px that represent the photo-switching reporters on a heterogeneous background. The background image is taken from an image (cropped to contain only areas of the sample) of the last pulse of the first OFF-switching cycle from the experimental dataset of the mouse model. Each target object has homogeneous intensity. The ratio of the initial intensities between the three groups and the maximum intensity of the background is 2:1:1:5, meaning that the background signal is stronger than that of the reporters (which mimics scenario of a blood-rich sample). Each group has the same kinetic constant as one of the three rsOAPs used in the experiment. The forward model is used to generate measurements of a set of a total of 100 2D OA switching images of size (150×150)px. A level of 1% Gaussian white noise is added to the simulated measurements to mimic to the noise level in the experimental datasets (see Fig. S1 (a)).

We tested three reconstruction approaches, namely, least-square only (LS), least-square regularized with total variation on the spatial maps of each reporter (LS+TV), and least-square regularized with TV and additionally ℓ_1 among the reporters (LS+TV+ℓ_1). We compare in Fig. S4 the results of using these methods against the ground truth. In all the scenarios, the three groups of reporters are successfully extracted from the non-switching background which is well recovered with a perfect structural similarity index (SSIM) of 1.0, though the peak signal-to-noise ratio (PSNR) varies among different methods.

Without any regularization, the unmixing performs well only on the first group of reporters, which has the largest kinetic constant, achieving an SSIM of 0.9 out of 1. However, the algorithm struggles to separate the second and the third groups. This is indicated by the presence of

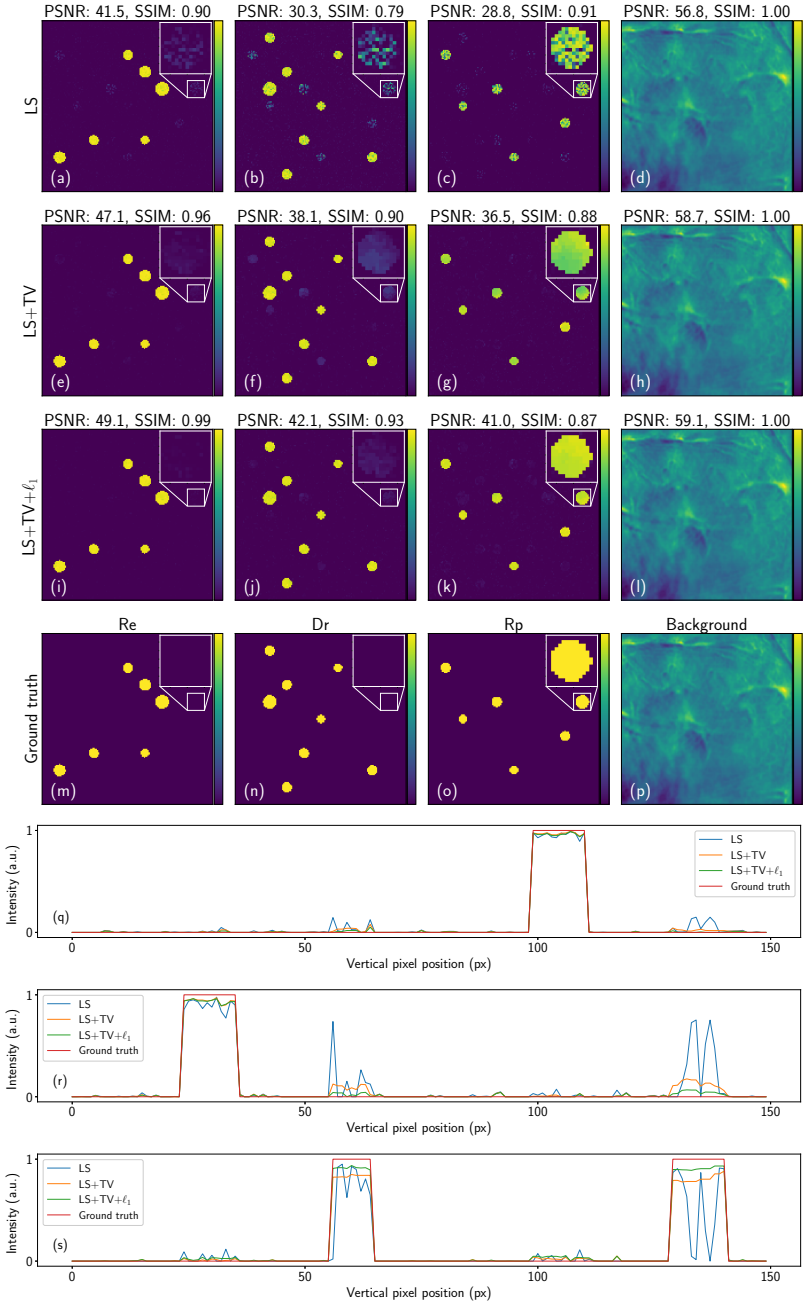

Fig. S4. Unmixing results of a simulated phantom of beads mimicking the experimental phantom. The first three rows each contains reconstructed distribution maps of the three rsOAPs shown in column one to three and the non-switching background image in the last column. The PSNR and SSIM of each reconstruction is indicated on top of each image. Row one (a)-(d): least-square solution. Row two (e)-(h): least-square with total variation regularization. Row three (i)-(l): least-square with total variation and ℓ_1 regularization. Row four (m)-(p): ground truth. (q)-(s): horizontal intensity profiles at the 60th row of pixels of the reporter Re (q), Dr (r), and Rp (s) for each reconstruction method. The intensities of all images are normalized to $[0, 1]$ for visual comparison.

reporters belonging to the third group appearing in the map of the second, leading to an SSIM of only 0.79 for the second group.

In fact, reporters of the third group "bleed" into the maps of the first two groups (see the

zoomed-in area in Fig.S4 (a) and (b)). After having added a TV regularizer for each group and tuned the regularization weights, we observe in Fig. S4 (e)-(g) that TV not only reduces noise inside the beads, giving a much smoother intensity distribution for each of them, but also greatly mitigates the bleed-through issue if we compare Fig. S4 (b) and (f). The PSNR of each group enjoys an average boost of 7dB due to the noise reduction and the SSIM of reporters Re and Dr is improved by 7% on average. However, there is still a hint of a remaining bleed-through in Fig. S4 (f), which is solved by the further addition of an ℓ_1 regularizer to enforce sparsity at each pixel. This proves to effectively solve the bleed-through problem and the intensity of each bead is more uniform, increasing the PSNR of each map by another 2-5dB (see Fig. S4 (i)-(k)).

To gain more insight on the reconstruction quality, we compare the intensity profiles along a representative horizontal line at the 60th row in Fig. S4 (q)-(s). We see that LS+TV+ℓ_1 outperforms LS only and LS+TV in the sense that, on one hand, the signal is correctly recovered at nearly its 100% intensity with very little fluctuation inside the bead (see signals at location 55px and 140px in Fig. S4 (s) for a good example) and that, on the other hand, LS+TV+ℓ_1 does not suffer from the bleed-through issue on locations where there should not be any signal compared to the other two approaches. Taking the signals at location 55px and 140px in Fig. S4 (q) and (r) as an example, LS only and LS+TV show relatively prominent peaks at these two locations where the signals from the third group should not appear at all, while LS+TV+ℓ_1 shows only flat tiny bumps. Hence, we conclude that our proposed reconstruction method, which combines TV and ℓ_1 regularization with least square, yields the best reconstruction results.

4. ESTIMATION OF THE KINETIC CONSTANTS

The kinetic constants $\bar{k}$ reported in Table S1 are measured experimentally and depend on the pulse energy and the subsequent unknown light fluence Φ_m during the measurement via $k = \frac{\bar{k}}{\Phi_m}$, where k is the intrinsic constant. To estimate Φ_m, we first use an empirical method to retrieve the decay rates $\{b_{\mathrm{Re}}, b_{\mathrm{Dr}}, b_{\mathrm{Rp}}\}$ of each species from the experimental dataset. Then, we determine Φ_m from

$$\Phi_m = \sqrt[3]{\frac{\bar{k}_{\mathrm{Re}}}{b_{\mathrm{Re}}} \frac{\bar{k}_{\mathrm{Dr}}}{b_{\mathrm{Dr}}} \frac{\bar{k}_{\mathrm{Rp}}}{b_{\mathrm{Rp}}}}, \tag{S11}$$

which is a cubic square root of the estimated results from all three species. To estimate the $\{b_{\mathrm{Re}}, b_{\mathrm{Dr}}, b_{\mathrm{Rp}}\}$, we fit an exponential function

$$y = a\mathrm{e}^{-bt} + c \tag{S12}$$

at each pixel to obtain a map of the decay rates b. Then, we approximate the OFF-switching rate of each reporter by locating the peaks in the histogram of the map of b. In Fig. S5(a), we show an example of the fitting result at one location inside each of the three rsOAPs marked by the three dots in Fig. S5(b) for the dataset of the experimental phantom of beads. In Fig. S5(c), we show the result of the empirical estimate of the kinetic constants. Three prominent peaks are observed, indicating the decay rates of the three species. We take a value around these peaks as the empirical estimate for $\{b_{\mathrm{Re}}, b_{\mathrm{Dr}}$ and $b_{\mathrm{Rp}}\}$. Plugging the estimated $\{b_{\mathrm{Re}}, b_{\mathrm{Dr}}, b_{\mathrm{Rp}}\}$ in Fig. S5 and $\bar{k}_{\mathrm{Re}}, \bar{k}_{\mathrm{Dr}}, \bar{k}_{\mathrm{Rp}}$ in Table S1 into Eq. (4), we obtain that $\Phi_m = 0.3$.

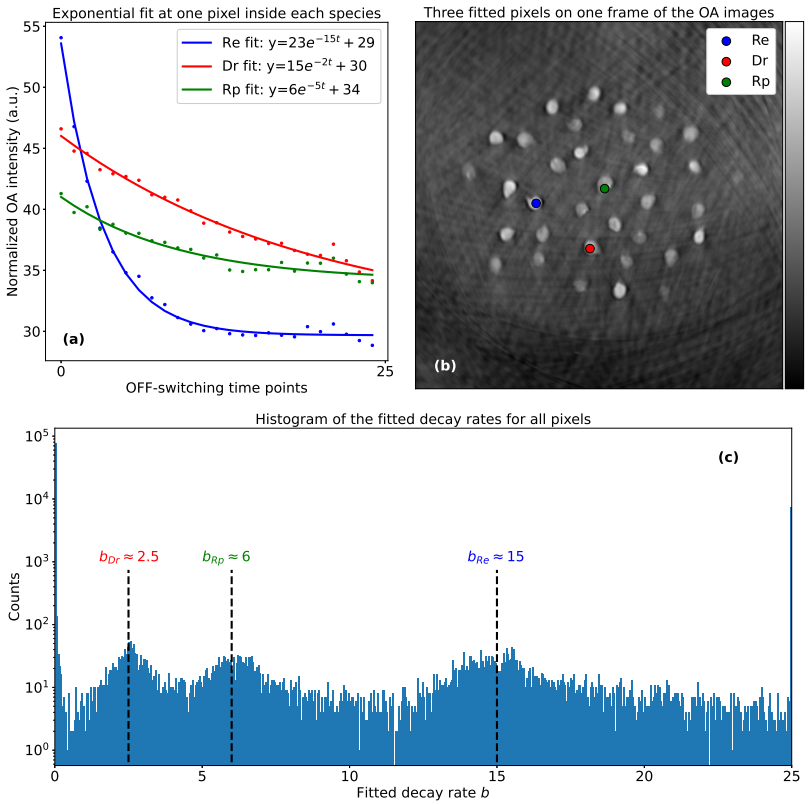

Fig. S5. Estimation of the decay rates for the three species based on the OFF-switching dataset of the experimental phantom of beads. (a) Fitting results at three representative pixels, each inside one of the three rsOAPs. The original data is the scatter points, the curves are the fitted results. (b) Location of the three pixels used in (a). The OA image is the first frame of the OFF-switching series. (c) Histogram (partial) of the fitted decay rate b for all the pixels in the OA image. Based on the fitting result in (a), only the part of the histogram where the values within the range (<25) is displayed.

REFERENCES

1. K. Mishra, M. Stankevych, J. P. Fuenzalida-Werner, *et al.*, "Multiplexed whole-animal imaging with reversibly switchable optoacoustic proteins," Sci. Adv. **6**, eaaz6293 (2020).
2. S. Prahl, "Tabulated molar extinction coefficient for hemoglobin in water," https://omlc.org/spectra/hemoglobin/summary.html. Accessed: 2024-10-18.
3. S. L. Jacques, "Optical properties of biological tissues: a review," Phys. Medicine Biol. **58**, R37–R61 (2013).
4. L. V. Wang and H.-i. Wu, *Biomedical optics: principles and imaging* (Wiley-Interscience, Hoboken, N.J, 2007). OCLC: ocm71427127.
5. H. Ammari, ed., *Mathematical Modeling in Biomedical Imaging II*, vol. 2035 of *Lecture Notes in Mathematics* (Springer Berlin Heidelberg, Berlin, Heidelberg, 2012).
6. C. Geuzaine and J. Remacle, "Gmsh: A 3-D finite element mesh generator with built-in pre- and post-processing facilities," Int. J. for Numer. Methods Eng. **79**, 1309–1331 (2009).
7. A. Logg, K. B. Ølgaard, M. E. Rognes, and G. N. Wells, "FFC: the FEniCS form compiler," in *Automated Solution of Differential Equations by the Finite Element Method,* vol. 84 of *Lecture Notes in Computational Science and Engineering* A. Logg, K. Mardal, and G. N. Wells, eds. (Springer, 2012), chap. 11.
8. M. S. Alnaes, J. Blechta, J. Hake, *et al.*, "The FEniCS project version 1.5," Arch. Numer. Softw. **3** (2015).